


**High-harmonic-generation spectra of HCN: A time-dependent density-functional-theory study**Xi Chu *Department of Chemistry and Biochemistry, The University of Montana, Missoula, Montana 59812, USA* (Received 23 January 2023; revised 17 April 2023; accepted 11 July 2023; published 24 July 2023)

This study examines the high-harmonic-generation spectra of hydrogen cyanide, focusing on the contrast between even and odd harmonics and their emissions under two opposite laser-molecule orientations. At lower energies, the emissions are higher when the potential energy of the hydrogen side is lowered, while at higher energies, the emissions are more pronounced when the potential energy of the nitrogen side is reduced. When the laser polarization aligns parallel to the molecular axis, the combined contributions of the  $\sigma$  and  $\pi$  orbitals result in a two-electron process, leading to varied intensity ratios between even and odd harmonics that a single active electron model cannot adequately explain.

DOI: [10.1103/PhysRevA.108.013116](https://doi.org/10.1103/PhysRevA.108.013116)**I. INTRODUCTION**

High-order harmonic generation (HHG) [1] based laser technology creates novel light sources [2–7] that are rapidly advancing ultrafast chemistry [8–10]. In addition, HHG itself functions as an attosecond probe [11,12]. As it becomes increasingly clear that features of harmonic spectra reflect multiorbital involvement [13–17], many-electron effects [18–20], interference [15,21–23], and resonances [15,24,25], time-dependent density-functional-theory (TDDFT) methods [26] are often adopted in HHG calculations.

For molecules without inversion symmetry, the effect of asymmetry on the HHG spectral features is studied by TDDFT calculations [27–30]. In a linearly polarized intense field, the even-to-odd harmonic intensity ratio is tunable by molecular orientation [28]. Furthermore, pure even harmonics whose polarization is perpendicular to the driving field are generated when the molecular axis of CO is perpendicular to the polarization of the driving laser [29]. The asymmetry also influences the spectral minimum caused by two-center interference of OCS when rescattering is oriented or if the process is separated into two half-optical cycles [30]. The asymmetry also influences the spectral minimum caused by two-center interference of OCS when rescattering is oriented or if the process is separated into two half-optical cycles [30]. Recently, the study of how even harmonic generation depends on the orientation was extended into the system of biased bilayer graphene [31].

Along the reaction path of isomerization from HCN to HNC, HHG spectra were calculated with the Lewenstein model to establish a relation between the spectral intensity and the stationary points on the reaction coordinates [32]. This scheme, however, may encounter problems with shape resonance as in photoelectron spectroscopy when analyzing isoelectronic molecules, including  $N_2$  [33], CO [34],  $C_2H_2$  [35], and HCN [36]. In the photoelectron measurement of  $N_2$ , shape resonance dominated by  $\sigma_u$  is about 10 eV above the  $X^2\Sigma_g^+$  state of  $N_2^+$  [37]. This feature is reproduced as enhanced HHG emissions from TDDFT calculations with fixed nuclear geometry at similar energies [38,39]. The calculation

paves the way for modeling coupled electron and nuclear dynamics for shape resonance in HHG.

The ground state for hydrogen cyanide is the  $X^1\Sigma^+$  state ( $1\sigma^2 2\sigma^2 3\sigma^2 4\sigma^2 5\sigma^2 1\pi^4$ ). Shape resonance enhances an autoionizing state converging to an increased ionization potential [36]. Among the four isoelectronic molecules, the electronic structure of HCN is unique because of the similar vertical ionization potentials corresponding to the two lowest electronic states of the ion,  $X^2\Pi$  ( $1\pi^{-1}$ ) and  $A^2\Sigma^+$  ( $5\sigma^{-1}$ ), which indicate the possible involvement of both states in rescattering. When the laser polarization is parallel to the molecular axis, the magnetic quantum numbers  $m$  and  $M$  are conserved. Hence, a process that involves removing or exciting an electron from both  $1\pi$  and  $5\sigma$  orbitals is a two-electron process

The two-electron and multiple orbital involvement further influences the HHG spectral features caused by asymmetry. In addition, it may impact the widely accepted HHG cutoff law [40,41] because it is based on a semi-classical analysis of a single active electron in an atomic system with inversion symmetry. In this work, we use a TDDFT method to examine these intriguing aspects of HHG of hydrogen cyanide, including the cutoff law, the even-to-odd harmonic intensity ratio, and the effects of the orientation of rescattering.

**II. FIELD-FREE ELECTRONIC STRUCTURE**

We start by expressing the initial 14-electron wave function of HCN as a Slater determinant of the occupied spin-orbitals of the ground state

$$\Psi(t = t_0) = \frac{1}{\sqrt{14!}} \det[\phi_1 \phi_2 \cdots \phi_{14}], \quad (1)$$

where  $t$  is time and  $t_0$  is the initial time. The field-free spin orbitals satisfy the static Kohn-Sham (KS) equation

$$\hat{H}^{(0)}(\mathbf{r})\phi_j(\mathbf{r}) = \epsilon_j \phi_j(\mathbf{r}), \quad j = 1, 2, \dots, 14, \quad (2)$$

where  $j$  is the spin-orbital index,  $\mathbf{r}$  is the spacial coordinate, and  $\hat{H}^{(0)}$  is the field-free Hamiltonian in which the  $LB_\alpha$  potential [42,43] is included.

TABLE I. Orbital energies ( $\epsilon$ ) of HCN and the ground-state occupation. The C-N distance is  $2.184 a_0$  [46] and the H-C distance is  $2.011 a_0$  [46]. The calculated electric dipole moment is  $1.213 ea_0$ , i.e., 3.084 Debye.

Orbital	$\epsilon$ (eV)	Occupation	Ion state	Vertical $I_p$ (eV)
$8\pi$	-2.198	0		
$7\sigma$	-3.114	0		
$6\sigma$	-4.128	0		
$2\pi$	-5.793	0		
$1\pi$	-13.617	4	$X^2\Pi$	13.607 [47]
$5\sigma$	-13.764	2	$A^2\Sigma^+$	14.011 [47]
$4\sigma$	-19.586	2	$B^2\Sigma^+$	19.06 [48]
$3\sigma$	-27.307	2		

The ground state is a singlet state, i.e., spin unpolarized, and the spin quantum number is conserved in the field. The set of spin orbitals is obtained by solving the KS equation with a generalized pseudospectral method [44,45]. The maximum distance to the nuclear charge center is set to be  $300 a_0$ . We use 9600 unevenly distributed grid points per plane that contains the molecule axis, with axial symmetry conserved in our calculations. The grid points are denser at the nuclear centers.

The occupied orbitals, their occupation, and the calculated orbital energies are given in Table I. They are compared to measured vertical ionization potentials. The measured energies for removing an electron from the highest occupied molecular orbital (HOMO) ( $1\pi$ ) and HOMO-1 ( $5\sigma$ ) differ only by 0.4 eV [47], indicating that the electrons occupying both orbitals may be active in an intense field. The negative of the calculated energies agrees well with the vertical ionization potentials. From the linear combination of atomic orbitals (LCAO) point of view,  $1\pi$  primarily consists of the linear combination of  $2p_x$  and  $2p_y$  orbitals of C and N, whereas  $5\sigma$  is mainly  $2p_z$  of N.

According to the same measurement, the transition energies of  $4\sigma \rightarrow 2\pi$  and  $4\sigma \rightarrow 6\sigma$  are 15.2 eV and 16.6 eV, respectively. The corresponding orbital energy differences from our calculations are 13.8 eV and 15.4 eV, respectively.

The calculated electron density distribution in HCN molecule creates a permanent dipole moment of 3.08 D, consistent with a measured value of 2.93 D [49]. The electron density is distributed towards cyanide and away from hydrogen. The two degenerate  $1\pi$  orbitals (HOMO) are occupied by four electrons. As shown in Fig. 1(d), their density is mainly near the cyanide end, contributing positively to the dipole moment. On the other hand, the combined contributions of the  $5\sigma$  (HOMO-1) and  $4\sigma$  (HOMO-2) orbitals are negative, as some of their electron densities are near the hydrogen atom [Fig. 1(b)]. The core orbitals and  $3\sigma$  orbital [Fig. 1(a)] contribute positively to the dipole moment.

### III. DIPOLE MOMENT IN A LASER PULSE

The time-dependent (TD) KS equation is

$$i\hbar \frac{\partial}{\partial t} \psi_j(\mathbf{r}, t) = [\hat{H}^{(0)}(\mathbf{r}) + \Delta v(\mathbf{r}, t) - e\mathbf{E}(t) \cdot \mathbf{r}] \psi_j(\mathbf{r}, t), \quad (3)$$

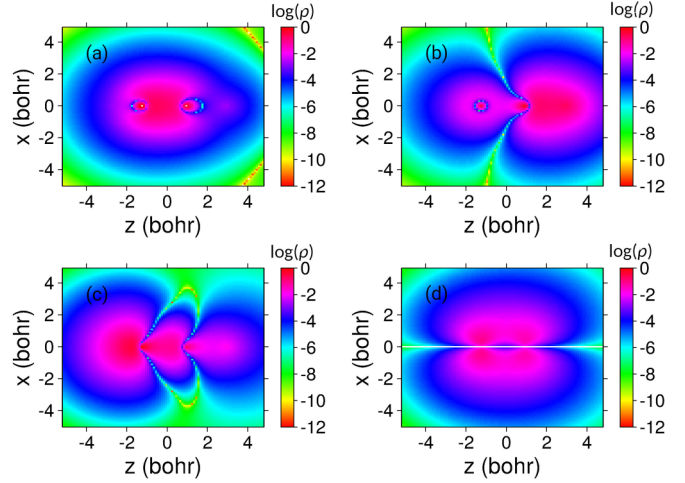


FIG. 1. Density in log scale of an electron in a (a)  $3\sigma$ , (b)  $4\sigma$ , (c)  $5\sigma$ , and (d)  $1\pi$  orbital of HCN. The Cartesian coordinates of N, C, and H are  $(0, 0, -1.236a_0)$ ,  $(0, 0, 0.949a_0)$ , and  $(0, 0, 2.959a_0)$ , respectively.

where  $\mathbf{E}$  is the electric field of the laser and  $\Delta v$  is the induced potential.

The polarization is along the  $z$  axis and

$$E(t) = f(t) \sin \omega_0 t, \quad (4)$$

where  $\omega_0$  is the angular frequency of the incident light and  $f(t)$  is the field strength

$$f(t) = F \sin^2 \frac{\omega_0 t}{40}, \quad 0 \leq t \leq 20T, \quad (5)$$

and  $T = 2\pi/\omega_0$  is an optical cycle.

The set of occupied spin orbitals is evolved by solving Eq. (3) with the generalized pseudospectral method [45], which is applied in the structural calculations with the same spatial grid. We adopt a split operator method to propagate the TD orbitals. An absorbing boundary is placed at  $120 a_0$  from the nuclear charge center and the maximum distance is  $300 a_0$ . The time step is 0.1 atomic units (2.419 attoseconds). The Fourier transform of the induced dipole moments is converged to the sixth decimal place at harmonics of the incident light. The TD dipole moment is determined as

$$d(t) = -e \iiint \rho(\mathbf{r}, t) z d^3\mathbf{r} \quad (6)$$

$$= -e \sum_{i=1}^{14} \langle \psi_i(\mathbf{r}, t) | z | \psi_i(\mathbf{r}, t) \rangle. \quad (7)$$

We plot the TD dipole moment in Fig. 2(a). Setting the nuclear charge center as the origin of coordinates and thus neutralizing the nuclear contribution to the dipole moment, we count contributions of the TD molecular orbitals with the occupation numbers included. The total transient dipole moment is in the solid blue line. The red and black curves are, respectively,  $1\pi$  and  $5\sigma + 4\sigma$  contributions. The red and black curves share similar oscillation amplitude and are spatially separated. The reason to count  $5\sigma$  and  $4\sigma$  together is that the dynamics of the two TD orbitals do not reflect the pulse shape [Fig. 2(b)].

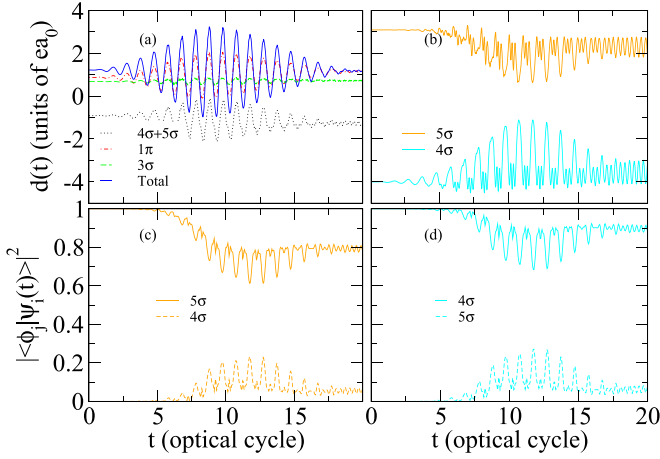


FIG. 2. (a) The induced dipole moment of HCN in a laser with intensity of  $3 \times 10^{14}$  W/cm<sup>2</sup>, calculated using the TDDFT method. HCN is at its equilibrium geometry and the laser is linearly polarized parallel to the molecular axis. The wavelength of the laser is  $\lambda = 800$  nm and the pulse length is 20 optical cycles. (b) Contributions of the TD  $5\sigma$  and  $4\sigma$  orbitals to the transient dipole moment. (c) Projections of the TD  $5\sigma$  orbital onto the field-free  $5\sigma$  and  $4\sigma$  orbitals. (d) Projections of the TD  $4\sigma$  orbital onto the field-free  $4\sigma$  and  $5\sigma$  orbitals.

The TD orbital density of  $1\pi$  is mostly between C and N, thus its dipole moment is mainly positive. While  $5\sigma$  is predominantly near N,  $4\sigma$  has a significant component of the  $1s$  orbital of H. In an intense laser field with polarization parallel to the molecular axis, the TD orbital  $\psi_{5\sigma}$  initially consists solely of the field-free  $5\sigma$  orbital. However, it periodically transfers some population to the field-free  $4\sigma$  orbital and vice versa, as observed in Fig. 2(c) and 2(d). These figures display  $|\langle 5\sigma(\mathbf{r})|\psi_{5\sigma}(\mathbf{r}, t)\rangle|^2$  and  $|\langle 4\sigma(\mathbf{r})|\psi_{5\sigma}(\mathbf{r}, t)\rangle|^2$ , as well as  $|\langle 5\sigma(\mathbf{r})|\psi_{4\sigma}(\mathbf{r}, t)\rangle|^2$  and  $|\langle 4\sigma(\mathbf{r})|\psi_{4\sigma}(\mathbf{r}, t)\rangle|^2$ , respectively. It is important to note that this exchange of population between occupied orbitals does not alter the density and therefore does not affect the calculated properties. In other words, neither the TD orbital  $\psi_{5\sigma}$  nor the TD orbital  $\psi_{4\sigma}$  accurately represent the dynamics of a single electron.

#### IV. HHG SPECTRA AND ANALYSIS

The HHG spectral density is given by

$$S(\omega) = \frac{3\omega^4}{2\pi c^3} |d(\omega)|^2, \quad (8)$$

where  $c$  is the speed of light and  $d(\omega)$  is the Fourier transform of the TD dipole moment

$$d(\omega) = \frac{1}{t_f - t_i} \int_{t_i}^{t_f} d(t) e^{-i\omega t} dt. \quad (9)$$

To examine the impact of bound and continuum states on the near-threshold harmonics, we employ two state filters represented by the operator  $\hat{F} = \sum_{j=1}^N s_j |\phi_j\rangle \langle \phi_j|$ . These filters are applied to the 14 TDKS orbitals at each time step in solving the TDKS equations Eq. (3). The operator  $\hat{F}$  is unitary when  $s_j = 1$  for  $j = 1 \dots N$ , representing a complete set. In our calculation, we set  $N = 9600$ .

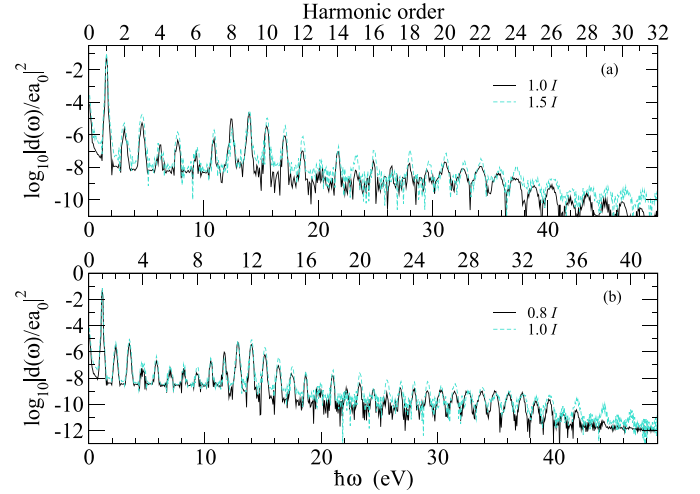


FIG. 3. The calculated HHG spectra of HCN in (a) 800-nm and (b) 1064-nm linearly polarized  $\sin^2$  laser pulses of 20 optical cycles. The laser polarization is parallel to the molecular axis. The laser intensities are given in the legends in which  $I = 10^{14}$  W/cm<sup>2</sup>.

For the first filter  $\hat{F}_i$ , we remove the free-electron components whose energies fall within the range of 0 to 0.4 eV, with 0 eV corresponding to the ionization threshold. This removal disrupts the three-step process, as these components are crucial for the electron's propagation and the acquisition of higher kinetic energies.

In the case of the second filter  $\hat{F}_{ii}$ , we eliminate the near-threshold boundstate components with energies ranging from  $-0.4$  to 0 eV.

In summary, for  $\hat{F}_i$ ,  $s_j = 0$  if  $\epsilon_j \in (0, 0.4$  eV) and  $s_j = 1$  otherwise. Similarly, for  $\hat{F}_{ii}$ ,  $s_j = 0$  if  $\epsilon_j \in (-0.4, 0$  eV), and  $s_j = 1$  otherwise.

#### A. Results

The calculated HHG spectra of HCN are presented for two different laser intensities at 800 nm and two intensities at 1064 nm, as shown in Fig. 3. In the energy range below 10 eV, the intensities of odd harmonics are higher than even harmonics in all cases. However, between 19 and 30 eV, the trend reverses, and the even harmonics become higher than the neighboring odd harmonics. This is particularly evident in the 800-nm laser at an intensity of  $10^{14}$  W/cm<sup>2</sup>, where H13 (20.4 eV) has a harmonic intensity one order of magnitude lower than H12 or H14. Similarly, in the  $1.5 \times 10^{14}$  W/cm<sup>2</sup> laser, the harmonic intensity of  $\sigma$  (26.4 eV) is 16 times lower than H16 and H17. The plateau region extends beyond 30 eV in the  $10^{14}$  W/cm<sup>2</sup> 1064-nm laser, leading to different even-odd patterns in different sections.

The obtained spectra are in agreement with the cutoff law [50]. In Fig. 3(a), the black curve shows a cutoff at 34.1 eV (H22), beyond which the harmonic intensity decays exponentially. The turquoise curve indicates a cutoff at 40.5 eV (H26). In comparison the cutoff law predicts values of 32.5 (H21) and 42.0 (H27) eV, respectively. Similarly, in Fig. 3(b), the cutoff energies are 40.8 eV (H35) and 47.1 eV (H40) for the two intensities, matching the predictions of the cutoff law.

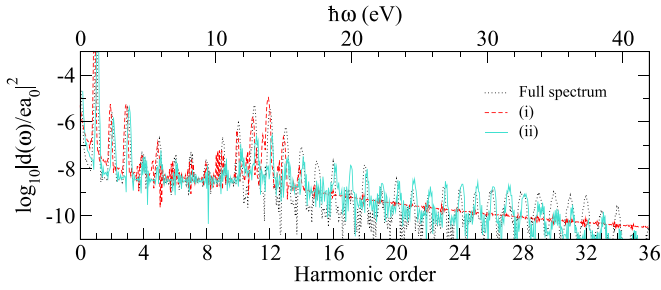


FIG. 4. Comparison of the HHG spectra with different field-free component removals. In (i), the field-free components between 0 and 0.4 eV are removed, where 0 eV represents the ionization threshold. In (ii) the field-free components between  $-0.4$  eV and 0 eV are removed. The spectra of (i) and (ii) are compared to the full spectrum obtained with a 1064-nm laser at an intensity of  $8 \times 10^{13}$  W/cm<sup>2</sup> in the upper panel.

Across all four spectra, the highest peak occurs near the ionization threshold at 14 eV. In the energy range of 10 to 17 eV, the harmonic intensity increases with the harmonic order, reaching a maximum near the ionization potential before decreasing. There is no clear even-odd contrast between neighboring peaks in this region.

To further investigate the influence of bound and free-electron states, state filters  $\hat{F}_i$  and  $\hat{F}_{ii}$  are applied. The spectrum

labeled as (i) in Fig. 4 is obtained by removing free-electron states above 17 eV, causing harmonics of 17 eV and above to disappear. The intensities of H9-H11 and H13 are reduced by about a factor of 3 below 17 eV. Spectrum (ii) in Fig. 4 shows the result when high Rydberg states are removed. It exhibits a plateau similar to the full spectrum, but the intensities of H9 to H14 are reduced by a greater factor of 9 to 20 near the ionization threshold.

Figure 5 displays the contributions of the  $\sigma$  (red) and  $\pi$  (turquoise) orbitals, along with the full spectrum (black). At the low-energy end, the  $\sigma$  contribution dominates, while between 8 eV and 16 eV, the  $\pi$  part often surpasses the total harmonic intensity, indicating some degree of cancellation between the  $\sigma$  and  $\pi$  contributions. In the range of 19 to 26 eV, the  $\pi$  contribution does not exhibit a clear even-odd contrast, whereas the  $\sigma$  contribution shows higher odd harmonics. In contrast, odd harmonics are lower or minimized in the full spectrum.

The HHG process in HCN is a two-electron process, with both  $\pi$  and  $\sigma$  contributions being significant around 20 eV, as shown in Fig. 5. However, despite their significance, the emission intensity is notably lower, suggesting an out-of-phase relationship and cancellation of the two contributions at 20 eV in all four panels of Fig. 5.

Beyond 26 eV, the  $\pi$  contribution diminishes into oscillations near the baseline, while the  $\sigma$  contribution

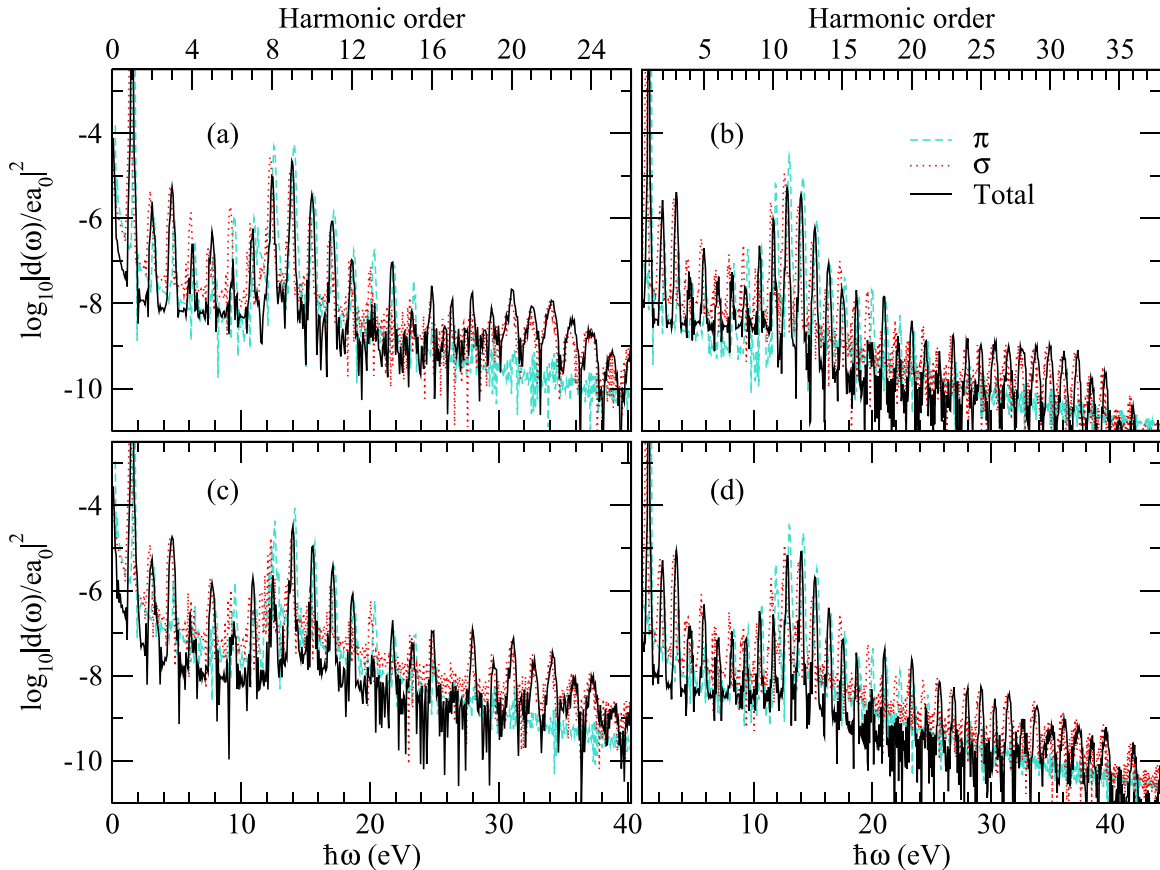


FIG. 5. The  $\sigma$  and  $\pi$  contributions to the HHG spectrum of HCN in 20 optical-cycle  $\sin^2$  pulses. The  $\sigma$  contribution is shifted slightly to the left and the  $\pi$  contribution to the right. (a)  $I = 10^{14}$  W/cm<sup>2</sup>,  $\lambda = 800$  nm; (b)  $I = 8 \times 10^{13}$  W/cm<sup>2</sup>,  $\lambda = 1064$  nm; (c)  $I = 1.5 \times 10^{14}$  W/cm<sup>2</sup>,  $\lambda = 800$  nm; (d)  $I = 10^{14}$  W/cm<sup>2</sup>,  $\lambda = 1064$  nm.

dominates harmonic emissions, even though  $1\pi$  is the HOMO.

### B. Discussion

HHG in the energy range of 10 to 17 eV exhibits an apparent enhancement in harmonic intensity. This enhancement can be attributed to multiphoton resonances between the ground and Rydberg states. Previous studies observed that high intensities can be achieved with moderate driving lasers, indicating the possibility of resonance effects [25,51]. In our spectra, we observe that the emission at 12 eV is more intense for the weaker driving laser, suggesting resonance effects in the weaker lasers. Enhanced recombination following both short and long trajectories may contribute to this effect [52]. However, below-threshold harmonics such as H10 and H11, which imply negative energy return upon recombination, are likely initiated by over-the-barrier ionization or tunneling followed by a long trajectory [53].

Figure 4 provides further insights into the role of resonances in the enhanced harmonics between 10 and 17 eV. It indicates that resonances involving Rydberg states play a more significant role in these harmonics compared to the contributions from free-electron states. On the other hand, the generation of harmonics above 17 eV does not involve these high Rydberg states, suggesting different underlying mechanisms.

Interestingly, beyond 26 eV, the  $\sigma$  contribution becomes dominant in harmonic emissions, despite  $1\pi$  being the HOMO. This can be explained by the favorable orientation of the  $\sigma$  TD orbitals when the field polarization is parallel to the molecular axis in the high-energy range.

The absence of a significant  $\pi$  contribution in this energy range suggests that single-electron dynamics likely dominate the near-cutoff harmonics. This is supported by the agreement between the calculated cutoff energy and the predictions of the cutoff law based on the single active electron approximation.

A striking feature present in all four spectra is the even-odd contrast between 19 and 26 eV. At 20 eV, in particular, the harmonic intensity is low despite both the  $\sigma$  and  $\pi$  contributions being high. This suggests that the out-of-phase contributions of  $\sigma$  and  $\pi$  result in low intensities of odd harmonics in this energy range.

### V. TIME-FREQUENCY ANALYSIS

We utilize a wavelet transform [38,54] of the TD dipole moment  $d(t)$  to obtain the time profile of the  $n$  th order harmonic

$$d_n(t) = \sqrt{\frac{\omega}{\tau}} \int d(t') e^{-\frac{\omega^2(t'-t)^2}{2\tau^2}} e^{-i\omega(t'-t)} dt', \quad (10)$$

where the wavelet window function depends on the frequency  $\omega = n\omega_0$ , while the total number of oscillations within the window is held constant and proportional to  $\tau$ . The specific values of  $d_n(t)$  vary slightly, but the shape and pattern of the modulus of a time profile are consistent for  $\tau$  values between 5 and 15, which is what we draw insights from. In the data presented, we set  $\tau = 5$ .

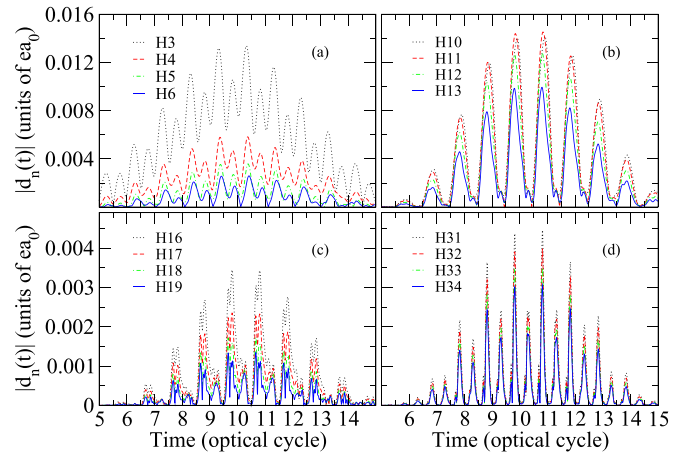


FIG. 6. Time profiles of selected harmonics generated in a 1064-nm  $8 \times 10^{13}$  W/cm<sup>2</sup> laser.

The polarization direction of the field changes every half-optical cycle, meaning  $\mathbf{E}(t + T/2) \approx -\mathbf{E}(t)$ . The slight difference between  $\mathbf{E}(t + T/2)$  and  $-\mathbf{E}(t)$  lies in the pulse shape  $f(t)$ . The time profile, therefore, shows how the molecular orientation relative to the polarization direction affects the harmonic emission by providing a comparison between  $|d_n(t)|$  and  $|d_n(t + T/2)|$ . Moreover, we can subsequently link this orientation dependence to molecular structure, as the external field included in Eq. (3) is  $-\mathbf{e}\mathbf{E}(t) \cdot \mathbf{r} = -ez(\mathbf{r})f(t) \sin \omega_0 t$ , which lowers the electronic potential on the H side in the first half of the optical cycle and that on the N side in the second half.

### A. Results

In Fig. 6, we present the time profiles of harmonics grouped by their photon energy and the mechanism of HHG. In Fig. 6(a), the curves for H3-H6 exhibit two peaks per optical cycle. The emissions are more intense when the laser field lowers the potential energy on the hydrogen side of the molecule.

Harmonics near the ionization threshold display a single broad peak per optical cycle, as shown in Fig. 6(b). Since the magnitude of the electric field  $|E(t)|$  also peaks twice per optical cycle, the bursts of a harmonic lose their correlation with the periodicity of the field. Time profiles for the same harmonics calculated with the two state filters applied are presented in Fig. 7. When some free-electron states are removed, as in Fig. 7(i), the peak values are similar to those in Fig 6(b), and there is still one broad peak per optical cycle, although the shape may differ. The peaks shift from near  $(m + 0.9)T$  to  $(m + 0.5)T$ , where  $m$  is an integer. On the other hand, removing some high Rydberg states significantly reduces the peak values in Fig. 7(ii). For H10 and H11, there are now two peaks per optical cycle, whereas for H12 and H13, the higher peaks further split into two, resembling plateau harmonics.

Figure 6(c) displays the time profiles of four harmonics within the plateau region. As is typical for this region, there are two peaks every half cycle. Unlike at the low-energy end, the peaks are higher when the potential energy is lowered on the nitrogen side of the molecule. The magnitude of  $|d_n(t)|$

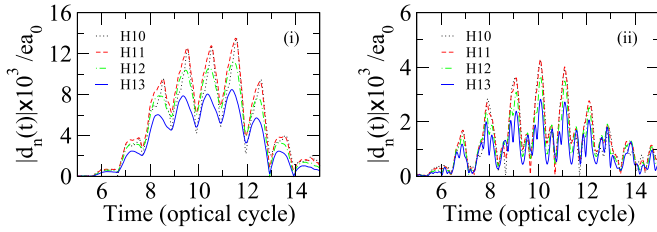


FIG. 7. Time profiles of H10-H13 with state filters applied. (i) Field-free components between 0 and 0.4 eV are removed, where 0 eV corresponds to the ionization threshold. (ii) Field-free components between  $-0.4$  eV and 0 eV are removed. The profiles demonstrate the effect of the field-free components on the harmonic emissions.

decreases as the harmonic order increases. However, it is worth noting that  $\sigma$  (20 eV) has lower harmonic intensity compared to H17 and H19, despite having a higher magnitude of the time profile, as depicted in the red curve of Fig. 5(b). This indicates that the phase of  $d_{17}(t)$  plays a critical role in reducing the intensity, as it is related to the integral of  $d_{17}(t)$  over time. In other words, there is an out-of-phase relationship among the different peaks in the time profile of  $\sigma$ .

Figure 8 further analyzes the time profile of  $\sigma$  by separating its  $\sigma$  and  $\pi$  contributions, i.e.,  $d_{17}(t) = d_{17\sigma}(t) + d_{17\pi}(t)$ . The absolute values of the two contributions are plotted together with  $|d_{17}(t)|$ . When the potential energy on the hydrogen side is lowered, the  $\sigma$  contribution is higher than the  $\pi$  contribution. As a result, in the first half cycle,  $|d_{17}(t)| \approx |d_{17\sigma}(t)| - |d_{17\pi}(t)|$ , leading to  $d_{17}(t)$  taking the sign of  $d_{17\sigma}(t)$ . In the second half cycle, it takes the sign of the  $\pi$  contribution. This pattern exists in all the harmonics in the energy range between 19 and 25 eV.

Figure 6(d) displays the time profiles of near-cutoff harmonics. The presence of two narrow peaks per cycle agrees with the semi-classically predicted single-electron trajectory for this energy range. The phases at recombination, represented by  $\omega_0 t_r$  at the peaks, are  $115^\circ$  and  $293^\circ$ , which differ

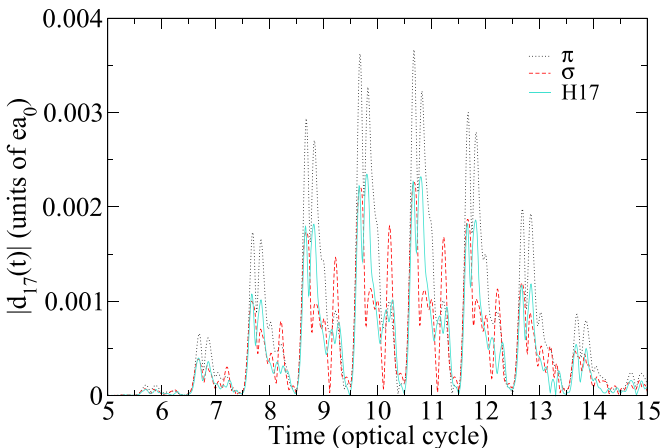


FIG. 8. Time profiles of the  $\sigma$  and  $\pi$  contributions to  $\sigma$  in a 1064-nm  $8 \times 10^{13}$  W/cm<sup>2</sup> laser.

from the values obtained by ignoring ion-electron interactions [41].

## B. Discussion

The low-energy HHG mechanism is multiphoton in nature. According to TD perturbation theory, the intensity of the  $n$ th harmonic radiation of a single molecule is proportional to the  $n$ th power of the irradiance, where the hyperpolarizability tensor  $\alpha^{(n)}(-n\omega_0, \omega_0)$  plays a crucial role. In particular,  $\alpha^{(2)}$  describes the second-order contribution and is given by a summation over excited states with terms involving excitation energies, photon energies, and transition dipole moments [55]. Similarly, higher-order hyperpolarizabilities such as  $\alpha^{(3)}$  [55] and  $\alpha^{(5)}$  [56] involve more excited states and become more complex. These excitations associated with  $n$ -photon absorption are also present in TDDFT calculations. In Fig. 6(a), the time profiles of H3-H6 reveal the contribution of excited states that shift the electron density towards the hydrogen side. The modulus of these time profiles is consistent with the lower intensities observed for even harmonics.

The phase relationship between different harmonics is an important factor in determining their intensities. By subtracting the constant value of  $d(0)$  from the TD dipole moment  $d(t)$ , denoted as  $\tilde{d}(t)$ , the Fourier transform remains unchanged. In the case of odd harmonics,  $\tilde{d}(t)$  and  $\tilde{d}(t + T/2)$  have opposite signs, resulting in in-phase time profiles. This means that the intensity of an odd harmonic is associated with the average of the two profiles. However, for even harmonics,  $\tilde{d}(t)$  and  $\tilde{d}(t + T/2)$  are out of phase, leading to a difference between them and lower intensities compared to neighboring odd harmonics.

The near-threshold harmonics exhibit a unique single-peak-per-cycle profile. The high Rydberg states are primarily responsible for this profile, while the unbound free-electron states have an influence on the intensities and bursting times of harmonics such as H10-H13.

In the plateau region, the harmonic emissions in the two half cycles are in phase with the  $\sigma$  and  $\pi$  contributions, respectively. For even harmonics, the  $\sigma$  and  $\pi$  contributions are in phase between the two half cycles, while for odd harmonics, they are out of phase. This leads to a cancellation effect, resulting in lower intensities for odd harmonics compared to adjacent even harmonics. This phenomenon is discernible in the intensities of various harmonics in 800-nm and 1064-nm lasers, where odd harmonics exhibit reduced intensities relative to the adjacent even harmonics. Such correlation in two-electron dynamics is inherently beyond the scope of models based on the single active electron approximation.

## VI. SUMMARY AND CONCLUSION

The study investigates the HHG spectra of HCN under laser polarization parallel to the molecular axis. In this alignment, the response of a  $\sigma$  orbital and a  $\pi$  orbital involves two electrons. TD orbitals with  $\sigma$  and  $\pi$  symmetries exhibit distinct contributions to different energy regions of the HHG spectrum.

When the energy of a harmonic is below the ionization potential, the emission bursts are more pronounced during the

period when the laser field lowers the potential energy of the electrons on the hydrogen side. This asymmetry contributes to a higher overall intensity of odd harmonics compared to even harmonics at the lower energy end of the HHG spectrum.

Resonance with near-threshold Rydberg states enhances the harmonic emissions near the ionization potential. In these cases, there is no clear contrast between even and odd harmonics. The time profiles of these resonance-enhanced harmonics show a single broad peak per optical cycle.

A few electronvolts above the ionization potential, the  $\sigma$  and  $\pi$  contributions to HHG are out of phase until approximately 26 eV. The  $\pi$  contribution dominates when the laser field lowers the potential energy on the nitrogen side, while the opposite occurs when the potential energy on the hydrogen side is lowered. This leads to an opposite phase between the two half cycles of the laser and results in lower intensities of odd harmonics.

For harmonics with energy beyond 26 eV, the HHG process is primarily governed by the  $\sigma$  contributions and the distinction between even and odd harmonics becomes less noticeable. The cutoff energies obtained from TDDFT calculations are consistent with predictions from the three-step model. The emissions are more intense when the potential energy of the electrons on the nitrogen side is lowered by the laser field.

## ACKNOWLEDGMENTS

This work is supported by the National Science Foundation Award No. PHY-1506441, and we utilized the Extreme Science and Engineering Discovery Environment (XSEDE) Expanse Compute resources at the San Diego Supercomputer Center at UC San Diego through allocation TG-PHY210099.

- 
- [1] M. Lewenstein, P. Balcou, M. Y. Ivanov, A. L'Huillier, and P. B. Corkum, *Phys. Rev. A* **49**, 2117 (1994).
- [2] P. Antoine, A. L'Huillier, and M. Lewenstein, *Phys. Rev. Lett.* **77**, 1234 (1996).
- [3] P. Paul, E. Toma, P. Breger, G. Mullot, F. Auge, P. Balcou, H. Muller, and P. Agostini, *Science* **292**, 1689 (2001).
- [4] J. Li, X. Ren, Y. Yin, K. Zhao, A. Chew, Y. Cheng, E. Cunningham, Y. Wang, S. Hu, Y. Wu, M. Chini, and Z. Chang, *Nat. Commun.* **8**, 186 (2017).
- [5] X. Ren, J. Li, Y. Yin, K. Zhao, A. Chew, Y. Wang, S. Hu, Y. Cheng, E. Cunningham, Y. Wu, M. Chini, and Z. Chang, *J. Opt.* **20**, 023001 (2018).
- [6] K. Midorikawa, *Nat. Photon.* **16**, 267 (2022).
- [7] G. Fan, K. Legare, V. Cardin, X. Xie, R. Safaei, E. Kaksis, G. Andriukaitis, A. Pugzlys, B. E. Schmidt, J. P. Wolf, M. Hehn, G. Malinowski, B. Vodungbo, E. Jal, J. Luning, N. Jaouen, G. Giovannetti, F. Calegari, Z. Tao, A. Baltuska *et al.*, *Optica* **9**, 399 (2022).
- [8] J. Vura-Weis, C.-M. Jiang, C. Liu, H. Gao, J. M. Lucas, F. M. F. de Groot, P. Yang, A. P. Alivisatos, and S. R. Leone, *J. Phys. Chem.* **4**, 3667 (2013).
- [9] T. Schnappinger, D. Jadoun, M. Gudem, and M. Kowalewski, *Chem. Commun.* **58**, 12763 (2022).
- [10] A. D. Ross, D. Hait, V. Scutelnic, E. A. Haugen, E. Ridente, M. B. Balkew, D. M. Neumark, M. Head-Gordon, and S. R. Leone, *Chem. Sci.* **13**, 9310 (2022).
- [11] D. R. Tuthill, F. Mauger, T. D. Scarborough, R. R. Jones, M. B. Gaarde, K. Lopata, K. J. Schafer, and L. F. DiMauro, *J. Mol. Spectrosc.* **372**, 111353 (2020).
- [12] L. He, S. Sun, P. Lan, Y. He, B. Wang, P. Wang, X. Zhu, L. Li, W. Cao, P. Lu, and C. D. Lin, *Nat. Commun.* **13**, 4595 (2022).
- [13] B. K. McFarland, J. P. Farrell, P. H. Bucksbaum, and M. Gühr, *Science* **322**, 1232 (2008).
- [14] O. Smirnova, Y. Mairesse, S. Patchkovskii, N. Dudovich, D. Villeneuve, P. Corkum, and M. Y. Ivanov, *Nature (London)* **460**, 972 (2009).
- [15] A. Ferre, A. E. Boguslavskiy, M. Dagan, V. Blanchet, B. D. Bruner, F. Burgy, A. Camper, D. Descamps, B. Fabre, N. Fedorov, J. Gaudin, G. Geoffroy, J. Mikosch, S. Patchkovskii, S. Petit, T. Ruchon, H. Soifer, D. Staedter, I. Wilkinson, A. Stolow *et al.*, *Nat. Commun.* **6**, 5952 (2015).
- [16] K. A. Hamer, D. R. Tuthill, T. D. Scarborough, L. F. DiMauro, K. Lopata, K. J. Schafer, M. B. Gaarde, and F. Mauger, *Phys. Rev. A* **104**, 033114 (2021).
- [17] Z. Shu, H. Liang, Y. Wang, S. Hu, S. Chen, H. Xu, R. Ma, D. Ding, and J. Chen, *Phys. Rev. Lett.* **128**, 183202 (2022).
- [18] Z. Zhao, J. Yuan, and T. Brabec, *Phys. Rev. A* **76**, 031404(R) (2007).
- [19] S. Patchkovskii, Z. Zhao, T. Brabec, and D. M. Villeneuve, *Phys. Rev. Lett.* **97**, 123003 (2006).
- [20] X. Chu and G. C. Groenenboom, *Phys. Rev. A* **105**, 053110 (2022).
- [21] C. Vozzi, F. Calegari, E. Benedetti, J.-P. Caumes, G. Sansone, S. Stagira, M. Nisoli, R. Torres, E. Heesel, N. Kajumba, J. P. Marangos, C. Altucci, and R. Velotta, *Phys. Rev. Lett.* **95**, 153902 (2005).
- [22] A. T. Le, X. M. Tong, and C. D. Lin, *Phys. Rev. A* **73**, 041402(R) (2006).
- [23] A. J. Uzan, H. Soifer, O. Pedatzur, A. Clergerie, S. Larroque, B. D. Bruner, B. Pons, M. Ivanov, O. Smirnova, and N. Dudovich, *Nat. Photon.* **14**, 188 (2020).
- [24] C. Jin, J. B. Bertrand, R. R. Lucchese, H. J. Worner, P. B. Corkum, D. M. Villeneuve, A.-T. Le, and C. D. Lin, *Phys. Rev. A* **85**, 013405 (2012).
- [25] M. Chini, X. Wang, Y. Cheng, H. Wang, Y. Wu, E. Cunningham, P.-C. Li, J. Heslar, D. A. Telnov, S.-I. Chu, and Z. Chang, *Nat. Photon.* **8**, 437 (2014).
- [26] E. K. U. Gross and W. Kohn, *Adv. Quant. Chem.* **21**, 255 (1990).
- [27] J. Heslar, D. Telnov, and Shih-I. Chu, *Phys. Rev. A* **83**, 043414 (2011).
- [28] P. M. Kraus, O. I. Tolstikhin, D. Baykusheva, A. Rupenyan, J. Schneider, C. Z. Bisgaard, T. Morishita, F. Jensen, L. B. Madsen, and H. J. Wörner, *Nat. Commun.* **6**, 7039 (2015).
- [29] H. Hu, N. Li, P. Liu, R. Li, and Z. Xu, *Phys. Rev. Lett.* **119**, 173201 (2017).
- [30] F. Mauger, P. M. Abanador, T. D. Scarborough, T. T. Gorman, P. Agostini, L. F. DiMauro, K. Lopata, K. J. Schafer, and M. B. Gaarde, *Struct. Dyn.* **6**, 044101 (2019).

- [31] Y. Ren, L. Jia, Y. Zhang, Z. Zhang, S. Xue, S. Yue, and H. Du, *Phys. Rev. A* **106**, 033123 (2022).
- [32] N.-T. Nguyen, B.-V. Tang, and V.-H. Le, *J. Mol. Struct.* **949**, 52 (2010).
- [33] J. L. Dehmer, D. Dill, and S. Wallace, *Phys. Rev. Lett.* **43**, 1005 (1979).
- [34] J. A. Stephens, D. Dill, and J. L. Dehmer, *J. Phys. B* **14**, 3911 (1981).
- [35] Z. H. Levine and P. Soven, *Phys. Rev. Lett.* **50**, 2074 (1983).
- [36] D. M. P. Holland, A. C. Parr, and J. L. Dehmer, *J. Phys. B* **17**, 1343 (1984).
- [37] P. Baltzer, M. Larsson, L. Karlsson, B. Wannberg, and M. C. Göthe, *Phys. Rev. A* **46**, 5545 (1992).
- [38] X. Chu and G. C. Groenenboom, *Phys. Rev. A* **87**, 013434 (2013).
- [39] X. Chu and G. C. Groenenboom, *Phys. Rev. A* **93**, 013422 (2016).
- [40] K. J. Schafer, B. Yang, L. F. DiMauro, and K. C. Kulander, *Phys. Rev. Lett.* **70**, 1599 (1993).
- [41] P. B. Corkum, *Phys. Rev. Lett.* **71**, 1994 (1993).
- [42] R. van Leeuwen and E. J. Baerends, *Phys. Rev. A* **49**, 2421 (1994).
- [43] X. Chu and M. McIntyre, *Phys. Rev. A* **83**, 013409 (2011).
- [44] X.-M. Tong and Shih-I. Chu, *Phys. Rev. A* **57**, 452 (1998).
- [45] X. Chu and Shih-I. Chu, *Phys. Rev. A* **63**, 023411 (2001).
- [46] G. Herzberg, *Electronic Spectra and Electronic Structure of Polyatomic Molecules* (Van Nostrand, New York, 1966).
- [47] C. Fridh and L. Asbrink, *J. Electron Spectrosc. Relat. Phenom.* **7**, 119 (1975).
- [48] D. Frost, S. Lee, and C. McDowell, *Chem. Phys. Lett.* **23**, 472 (1973).
- [49] C. P. Smyth and K. B. McAlpine, *J. Am. Chem. Soc.* **56**, 1697 (1934).
- [50] J. L. Krause, K. J. Schafer, and K. C. Kulander, *Phys. Rev. A* **45**, 4998 (1992).
- [51] E. Toma, P. Antoine, A. de Bohan, and H. Muller, *J. Phys. B: At. Mol. Opt. Phys.* **32**, 5843 (1999).
- [52] S. Camp, K. J. Schafer, and M. B. Gaarde, *Phys. Rev. A* **92**, 013404 (2015).
- [53] J. A. Hostetter, J. L. Tate, K. J. Schafer, and M. B. Gaarde, *Phys. Rev. A* **82**, 023401 (2010).
- [54] C. K. Chui, *An Introduction to Wavelets* (Academic, New York, 1992).
- [55] D. P. Craig and T. Thirunamachandran, *Molecular Quantum Electrodynamics: An Introduction to Radiation-Molecule Interactions* (Dover, New York, 1998).
- [56] J. Reintjes, C.-Y. She, and R. Eckardt, *IEEE J. Quantum Electron.* **14**, 581 (1978).